

Almost Analytic Models of Ultramagnetized Neutron Star Envelopes

Jeremy S. Heyl* Lars Hernquist†

June 11, 2021

Lick Observatory, University of California, Santa Cruz, California 95064, USA

Abstract

Recent ROSAT measurements show that the x-ray emission from isolated neutron stars is modulated at the stellar rotation period. To interpret these measurements, one needs precise calculations of the heat transfer through the thin insulating envelopes of neutron stars. We present nearly analytic models of the thermal structure of the envelopes of ultramagnetized neutron stars. Specifically, we examine the limit in which only the ground Landau level is filled. We use the models to estimate the amplitude of modulation expected from non-uniformities in the surface temperatures of strongly magnetized neutron stars. In addition, we estimate cooling rates for stars with fields $B \sim 10^{15} - 10^{16}$ G which are relevant to models that invoke “magnetars” to account for soft γ -ray emission from some repeating sources.

1 Introduction

Since the launch of the ROSAT satellite, our knowledge of isolated neutron stars has expanded into new realms. Before ROSAT, neutron stars were somewhat unique among astronomical objects. Although they had been observed over a range of energies from radio to ultra-high-energy gamma rays, and had been evoked to power a variety of astrophysical objects from pulsars to soft X-ray repeaters and gamma-ray bursts, one could not argue unequivocally that a single photon from the surface of a neutron star had ever been detected.

For the first time, we have direct evidence for radiation from the surfaces of neutron stars. More than a dozen such sources have been detected by ROSAT

*Current address: Theoretical Astrophysics, mail code 130-33, California Institute of Technology, Pasadena CA 91125, USA

†Presidential Faculty Fellow

Table 1: Several pulsars with observed surface blackbody emission

Pulsar	References
PSR J0437-4715	Becker & Trümper 1993
PSR 0630+18 (Geminga)	Halpern & Holt 1992, Halpern & Ruderman 1993 Halpern & Wang 1997
PSR 0656+14	Finley, Ögelman & Kiziloglu 1992, Anderson et al. 1993, Greiveldinger et al. 1996, Possenti, Mereghetti & Colpi 1996
PSR 0833-45 (Vela)	Ögelman, Finley & Zuckerman 1993
PSR 1055-52	Ögelman & Finley 1993, Greiveldinger et al. 1996
PSR 1929+10	Yancopoulos, Hamilton & Helfand 1994

(*e.g.* Ögelman 1995), and more than ten have been fitted with spectra. The spectra divide the objects into two classes: 1) objects with hard spectra whose X-ray emission is best attributed to the magnetosphere, and 2) neutron stars whose soft flux is well-described by a blackbody spectrum. Table 1 lists several of those that fall into the second group with pertinent references.

The X-ray spectra of these objects consist of a soft blackbody and hard power-law component. Generally, the surface temperature inferred from modeling the blackbody is approximately what one would expect for a cooling neutron star at the characteristic age of the pulsar. If this interpretation is correct, the observations provide a direct probe of the structure of cooling neutron stars. Furthermore, the observations show that the thermal radiation is modulated at the rotation period of the pulsars. A strong magnetic field can modulate the thermal flux by causing the heat conduction in the outer layers of the star to be anisotropic. Both to translate these observations into constraints on the structure of neutron stars and to understand modulation of the radiation, we must have a detailed understanding of the insulating layers of the neutron-star crust, *i.e.* the envelope.

We proceed in the spirit of Gudmundsson, Pethick & Epstein (1982) and concentrate our analysis on the thin region, the envelope, which insulates the bulk of the neutron star. The envelope is customarily defined to extend from zero density to $\rho \sim 10^{10}$ g/cm³, and its thickness (h_E) is of the order of tens of meters, very small compared to the radius of the star, $R \sim 10$ km. By limiting the analysis, we focus on how various physical processes affect the thermal structure of the envelope and the relationship between the core temperature and the flux emitted at the surface. An alternative point of view is to combine the envelope calculation with an estimate of the cooling rate due to neutrinos and the total heat capacity of the neutron star, yielding theoretical cooling curves

(*e.g.* Tsuruta et al. 1972, Nomoto & Tsuruta 1981, Glen & Sutherland 1980, Van Riper & Lamb 1981)

Several authors have made much progress in understanding the properties of neutron star envelopes with and without magnetic fields. Gudmundsson, Pethick & Epstein (1982) numerically calculate the thermal structure for unmagnetized envelopes, and Hernquist & Applegate (1984) present analytic models for the $B = 0$ case. Tsuruta (1979), Glen & Sutherland (1980), Van Riper & Lamb (1981) and Urpin & Yakovlev (1980) calculate the luminosity observed at infinity as a function of the core temperature for several magnetic field strengths less than 10^{14} G, including the zero-field case. Hernquist (1985) calculates the thermal structure of envelopes for $B \leq 10^{14}$ G for transport along the field, using the electron conductivities of Hernquist (1984) which account for the quantization of electron energies in the magnetic field in a relativistic framework. We will use these conductivities in the present work; therefore, Hernquist (1985) provides a natural benchmark.

Van Riper (1988) builds upon the Hernquist (1985) results by exploring various assumptions concerning the properties of the envelope at low densities and calculating profiles for many field strengths ($B < 10^{14}$ G) and core temperatures. Again, these calculations are limited to conduction along the field. Schaaf (1990), using the electron conductivities calculated in Schaaf (1988), calculates the thermal structure in two dimensions for $B \lesssim 10^{11}$ G. Above a field strength of 10^{12} G, the calculations are not considered reliable. Finally, Shibano et al. (1995) present the temperature distribution as a function of magnetic colatitude for $B = 10^{12}$ G from a numerical solution to the two-dimensional thermal structure equation in a plane-parallel approximation.

The current work complements the previous ones by extending the results to stronger field strengths (10^{14} G $\leq B \leq 10^{16}$ G) in a semi-analytical fashion. We apply the approach of Hernquist & Applegate (1984) in the limit of a strongly magnetized envelope, and then justify and use the plane-parallel approximation to solve the two-dimensional structure equation. We derive separable thermal structure equations in the high and low temperature limits for both liquid and solid material. We calculate the thermal structure in terms of simple (although analytically intractable) integrals.

The plane-parallel approximation has the second important advantage that the detailed field configuration separates from the thermal structure problem. Assuming that it is correct, we can synthesize the results for any field distribution $B(\theta, \phi)$ as long as B is not too inhomogeneous on the scale of the envelope thickness (*i.e.* $|B/\nabla B| \gg h_E$).

We find that the emission from a given surface element is a simple function of the location of the element. Using this functional form, we derive light curves and time-dependent spectra including general relativistic effects. Although we closely follow the formalism of Page (1995), we calculate the two-dimensional thermal structure of the envelope and present results for several field strengths

and fluxes. We internally verify and justify the geometric simplification used to translate our results into observables.

2 Preliminaries

In extremely intense magnetic fields, the Landau energy ($\hbar\omega_B$) of an electron will typically exceed its thermal energy. In these strong fields, the quantization of the electron energy determines the structure of the electron phase space and must be taken into account in calculating the thermodynamics of the electron gas.

In what follows, we will use the dimensionless units

$$\beta = \frac{\hbar\omega_B}{m_e c^2} = \frac{\hbar|e|\hbar}{m_e^2 c^3} B \approx \frac{B}{4.4 \times 10^{13} \text{ G}}, \quad (1)$$

$$\tau = \frac{kT}{m_e c^2} \approx \frac{T}{5.9 \times 10^9 \text{ K}} \text{ and } \zeta = \frac{\mu}{m_e c^2} \quad (2)$$

where μ is the chemical potential of the electron gas including the electron rest mass. Heyl (1998), Hernquist (1985), and Hernquist (1984) outline the techniques for calculating the thermodynamic properties of a magnetized electron gas, and we adopt their methodology for the remainder of the paper.

3 The Low-Temperature, Strong-Field Regime

We are specifically interested in the low temperature limit ($\tau \ll \zeta - 1$) and the regime in which only one Landau level is filled ($\zeta < \sqrt{2\beta + 1}$). For neutron stars with $\beta \gtrsim 1$, this limit applies to the regions that most effectively insulate the isothermal core of the star. We will use the results of Yakovlev (1984) and Hernquist (1984) to calculate the thermal conduction in the liquid and solid phases.

3.1 Degenerate Structure Equations

If we assume that the pressure is supplied by the electrons alone, the general relativistic equations of thermal structure in the plane-parallel approximation assume the simple form

$$\frac{dT}{d\mu} = \frac{F}{g_s} \frac{Y_e}{m_u} \frac{1}{\kappa} \left(1 - \frac{F}{g_s} \frac{S_e}{\rho\kappa} \right)^{-1} \quad (3)$$

$$\frac{d\mu}{dz} = \frac{m_u}{Y_e} g_s \left(1 - \frac{F}{g_s} \frac{S_e}{\rho\kappa} \right) \quad (4)$$

where we have neglected the thickness of the envelope ($h_E \sim 100 \text{ m}$) relative to the stellar radius (R). Here, m_u is the atomic mass unit, Z and A are the

mean atomic number and mean atomic mass of the material, ρ is the density of the matter, S_e is the entropy of the electron gas per unit volume, κ is the thermal conductivity, and F and g_s are the flux and the acceleration of gravity as measured at the surface, respectively. For completely ionized material, Y_e is given by the product of Z/A and the ionized fraction.

In the absence of a magnetic field, this plane-parallel approximation introduces errors of the order $R_s h_E / R^2 \approx 0.6\%$ where $R_s = 2GM/c^2$ (Gudmundsson, Pethick & Epstein 1982). To understand the potential errors of the plane-parallel treatment in the presence of a magnetic field, we compare the results of Shibanov et al. (1995) with those of Schaaf (1990). Although Shibanov et al. (1995) use a one-dimensional approach, their results agree with those of the two-dimensional calculations by Schaaf (1990) for several surface temperatures and a magnetic field of 10^{12} G. In stronger magnetic fields, conduction perpendicular to the magnetic field is even less important, and we expect the one-dimensional method to be even more accurate.

To estimate the errors in using the plane-parallel treatment in the presence of the magnetic field, we examine the thermal structure equation in two dimensions (Schaaf 1990)

$$\begin{aligned} \nabla \cdot \mathbf{F} = & -\frac{e^{-\Lambda_s}}{r^2} \frac{\partial}{\partial r} \left[r^2 \kappa_{11} e^{-\Lambda_s} \frac{\partial T}{\partial r} + r \kappa_{12} \frac{\partial T}{\partial \theta} \right] \\ & - \frac{1}{r \sin \theta} \frac{\partial}{\partial \theta} \left[\sin \theta \left(\kappa_{21} e^{-\Lambda_s} \frac{\partial T}{\partial r} + \frac{\kappa_{22}}{r} \frac{\partial T}{\partial \theta} \right) \right] = 0, \end{aligned} \quad (5)$$

where θ is an angle along the surface of star, specifically the magnetic colatitude,

$$e^{-\Lambda_s} = \sqrt{1 - \frac{R_s}{R}}, \quad (6)$$

and the κ_{ij} are the components of the thermal conduction tensor, where 1 denotes the radial direction and 2 denotes the tangential direction. The components of κ are found by rotating the tensor calculated by Hernquist (1984) and Yakovlev (1984) so that the z -direction locally coincides with the radial direction. This gives

$$\kappa_{11} = \kappa_{yy} \sin^2 \psi + \kappa_{zz} \cos^2 \psi, \quad (7)$$

$$\kappa_{22} = \kappa_{yy} \cos^2 \psi + \kappa_{zz} \sin^2 \psi, \quad (8)$$

$$\kappa_{12} = \kappa_{21} = (\kappa_{yy} - \kappa_{zz}) \sin \psi \cos \psi, \quad (9)$$

where ψ is the angle between the local field direction and the radial direction, and κ_{yy} and κ_{zz} respectively are the components of the heat conduction tensor perpendicular and parallel to the direction of the magnetic field.

For a uniformly magnetized neutron star $\psi = \theta$; for a dipole field, $\cot \psi = 2 \cot \theta$ (Greenstein & Hartke 1983), or more conveniently

$$\cos^2 \psi = \frac{4 \cos^2 \theta}{3 \cos^2 \theta + 1}. \quad (10)$$

If we assume that the components of the thermal conduction matrix (κ) are of the same order and take the maximum temperature gradient to be $T_c - T_{\text{eff}} \sim T_c$ radially over the thickness of the envelope, h_E , or tangentially over one radian, we obtain

$$\frac{\partial T}{\partial \theta} \sim T_c \ll e^{-\Lambda_s r} \frac{\partial T}{\partial r} \sim e^{-\Lambda_s R} \frac{T_c}{h_E} \sim 10^2 T_c \quad (11)$$

where T_c is the core temperature. We find that neglecting derivatives with respect to angle does not dramatically increase the error relative to the unmagnetized plane-parallel case.

However, this argument does not apply for θ close to $\pi/2$ (*i.e.* where the magnetic field lines are parallel to the surface for a uniform or dipole field). Here,

$$\kappa_{22} = \kappa_{zz} \gg \kappa_{11} = \kappa_{yy}. \quad (12)$$

If we reexamine the error analysis for $\psi \approx \pi/2$ we find that relevant quantities to compare are

$$\kappa_{22} \frac{\partial^2 T}{\partial \theta^2} \text{ and } \kappa_{11} r^2 e^{-2\Lambda_s} \frac{\partial^2 T}{\partial r^2}. \quad (13)$$

The tangential transport will exceed the radial transport if

$$\cos^2 \psi < e^{2\Lambda_s} \frac{h_E^2}{R^2} - \frac{\kappa_{yy}}{\kappa_{zz}} \quad (14)$$

Comparing these values we find that if $\kappa_{zz} \gtrsim 10^4 \kappa_{yy}$, the one-dimensional treatment will break down near $\psi = \pi/2$; otherwise, the plane-parallel treatment is adequate even at $\psi = \pi/2$.

For regions where the magnetic field lines are not nearly parallel to the surface, the plane-parallel approximation works well; consequently even for an arbitrary field geometry, because the envelope is thin, we ignore $\partial/\partial\theta$ terms in the structure equation compared to $r\partial/\partial r$ terms and focus on radial heat flow. With these assumptions, we have (Schaaf 1990)

$$\kappa = \kappa_{11} = \kappa_{zz} \cos^2 \psi + \kappa_{yy} \sin^2 \psi. \quad (15)$$

In the low-temperature limit, we obtain the dimensionless equation

$$\frac{d\tau}{d\zeta} = \left(Y_e \frac{F}{m_u g_s} \frac{\lambda_e^2}{c} \right) \left(\frac{ck}{\lambda_e^2} \frac{1}{\kappa} \right) \quad (16)$$

where λ_e is the electron Compton wavelength and the dimensionless flux is given by

$$\left(Y_e \frac{F}{m_u g_s} \frac{\lambda_e^2}{c} \right) = 7.83 \times 10^{-3} \frac{Z_{26} T_{\text{eff},6}^4}{A_{56} g_{s,14}}, \quad (17)$$

where $Z_{26} = Z/26$, $A_{56} = A/56$, $T_{\text{eff},6} = T_{\text{eff}}/10^6$ K, and $g_{s,14} = g_s/10^{14}$ cm/s². T_{eff} is the effective blackbody temperature of the neutron star photosphere again as measured at the surface, which we take to be located at an optical depth of $2/3$.

For Equation 16 to be separable for an arbitrary geometry, κ_{zz} and κ_{yy} must depend on τ in the same fashion. For electron-ion scattering this is the case, so we can hope to find a simple analytic solution to the structure equation. Unfortunately, since the cross-section for electrons to scatter off of phonons depends explicitly on temperature, in the solid state the structure equation is separable only where the field is either purely radial or tangential.

In the liquid state, we obtain the following structure equation,

$$\tau \frac{d\tau}{d\zeta} = \left(Y_e \frac{F}{m_u g_s} \frac{\lambda_e^2}{c} \right) \left[\cos^2 \psi \frac{\pi}{3} \frac{\beta^2}{Z \alpha^2} \frac{\phi_{ei}(\zeta; \beta)}{\sqrt{\zeta^2 - 1}} + \frac{\sin^2 \psi}{12\pi} \frac{Z \alpha^2}{\beta} Q_{ei}(\zeta; \beta) \sqrt{\zeta^2 - 1} \right]^{-1} \quad (18)$$

where α is the fine-structure constant. In the solid state for electron-phonon scattering, we obtain

$$\frac{d\tau}{d\zeta} = \left(Y_e \frac{F}{m_u g_s} \frac{\lambda_e^2}{c} \right) \left[\frac{1}{3} \frac{\beta^2}{\alpha u_{-2}} \phi_{ep}(\zeta; \beta) \right]^{-1}, \quad \psi = 0 \quad (19)$$

$$\tau^2 \frac{d\tau}{d\zeta} = \left(Y_e \frac{F}{m_u g_s} \frac{\lambda_e^2}{c} \right) \left[\frac{1}{12} \frac{\alpha u_{-2}}{\beta} Q_{ep}(\zeta; \beta) \right]^{-1}, \quad \psi = \frac{\pi}{2} \quad (20)$$

The functions ϕ and Q are defined and calculated in Yakovlev (1984) and Hernquist (1984) and we take $u_{-2} \approx 13$ (Yakovlev & Urpin 1980, Potekhin & Yakovlev 1996) for a body-centered cubic lattice.

4 The High Temperature Regime

In the nondegenerate regime we assume that most of the heat is transported by photons and that free-free absorption provides the opacity. We take the unmagnetized thermal conductivity to be of the Kramer's form (Silant'ev & Yakovlev 1980),

$$\kappa^{(F)} = \kappa_0 \frac{T^{13/2}}{\rho^2} \eta_{ff}(b, \psi) \quad (21)$$

where

$$\kappa_0 = \frac{1}{2.947} \frac{c_7}{\pi \sqrt{2\pi}} \frac{\sigma c k^{7/2} m_u^2 m_e^{3/2} A^2}{e^6 \hbar^2 Z^3} \quad (22)$$

$$= \frac{16\sigma}{3} \frac{m_u}{m_u} \frac{196.5 A^2}{24.59 Z^3} \frac{\text{g}}{\text{cm}^5 \text{K}^{7/2}}, \quad (23)$$

$c_7 = 316.8$, σ is the Stefan-Boltzmann constant and $b \equiv \beta/\tau$. The factor of 2.947 scales the results of Silant'ev & Yakovlev (1980) to agree with the results of Cox & Giuli (1968) (for discussion see Hernquist 1985).

We parameterize the effects of the magnetic field by the anisotropy factor for free-free absorption (η_{ff}). Absorption dominates the opacity through the nondegenerate portion of the envelope (Pavlov & Yakovlev 1977, Silant'ev & Yakovlev 1980). We use the analytic results of Pavlov & Yakovlev (1977) to extrapolate beyond the tabulated values in Silant'ev & Yakovlev (1980); *i.e.* for $b > 1000$. For $b < 1000$ we use the results of Silant'ev & Yakovlev (1980).

4.1 Non-degenerate Structure Equation

We follow the method of Hernquist & Applegate (1984), but we do not require that the conductivity be a power law in ρ and T .

In the non-degenerate regime, the thermal structure equation of the envelope is

$$\frac{dT}{dP} = \frac{F}{g_s} \frac{1}{\rho\kappa} \quad (24)$$

and we consider an unmagnetized conductivity which is a power law as Equation 21

$$\kappa = \kappa_0 \frac{T^\delta}{\rho^\alpha}. \quad (25)$$

Even in an intense magnetic field, in the nondegenerate regime, the pressure is given by the ideal gas law (Blandford & Hernquist 1982)

$$P = \frac{Y_e}{m_u} \rho k T. \quad (26)$$

We combine Equations 24–26 with Equation 21, yielding

$$\frac{dT}{dP} = \frac{F}{g_s} \frac{1}{\kappa_0} \left(\frac{m_u}{Y_e k} \right)^{\alpha-1} \frac{P^{\alpha-1}}{\eta_{ff}(b, \psi) T^{\alpha+\delta-1}}. \quad (27)$$

As for the structure equations in the degenerate limit, this equation is separable, yielding $\rho(T)$. Because η_{ff} depends on T through the argument b , the relation between T and P need not be a power law as in the unmagnetized case. In the limit that $\eta_{ff} = 1$, the result of Hernquist & Applegate (1984) obtains.

More generally, if we take, η_{ff} to be a power law $\propto b^{-2}$ (*e.g.* Tsuruta et al. 1972) which is approximately true for $b \rightarrow \infty$, we can immediately use the results of Hernquist & Applegate (1984) to obtain that the conductivity is constant along a solution through the nondegenerate envelope:

$$\kappa = \frac{\alpha + \delta - 2}{\alpha} \frac{F}{g_s} \frac{Y_e k}{m_u} \quad (28)$$

$$= 7.07 \times 10^{13} \frac{Z_{26}}{A_{56}} \frac{T_{\text{eff},6}^4}{g_{s,14}} \frac{\text{erg}}{\text{K cm s}} \quad (29)$$

for $\alpha = 2$ and $\delta = 6.5$ as in Equation 21. If we equate this result with our assumed conductivity and solve for T , we find that the solution follows

$$T = \left(\frac{\kappa}{a_\beta \kappa_0} \right)^{1/(\delta-2)} \rho^{\alpha/(\delta-2)} = 10^6 \text{K} \left(\frac{\rho}{\rho_{T_6}} \right)^{4/9} \quad (30)$$

where

$$a_\beta = \frac{2}{3} q \left(\frac{\beta m_e c^2}{k} \right)^2 \frac{1}{\ln b_{\text{Typical}}} \quad (31)$$

$$\rho_{T_6} = 71.3 \text{ g cm}^{-3} \frac{\beta}{\sqrt{\ln b_{\text{Typical}}}} A_{56}^{3/2} Z_{26}^{-2} T_{\text{eff},6}^{-2} g_{s,14}^{1/2}, \quad (32)$$

and b_{Typical} is a typical value of β/τ in the envelope, $b_{\text{Typical}} \approx 6 \times 10^3 \beta$. One should note that for free-free scattering in the weak-field limit, $T \propto \rho^{4/13}$.

With Equation 30, we can calculate the density at the onset of degeneracy. We will assume that at the onset of degeneracy the electron density is given by fully degenerate expression and that $\tau \approx \zeta - 1$. This yields

$$\rho_{\text{ND/D}} = 3.92 \times 10^5 \text{ g cm}^{-3} \beta (\ln b_{\text{Typical}})^{1/7} A_{56}^{6/7} Z_{26}^{-5/7} T_{\text{eff},6}^{4/7} g_{s,14}^{-1/7}. \quad (33)$$

In principle, electron scattering could also play a role in the nondegenerate regime. To simplify the calculation, we neglect its contribution and verify that it is indeed negligible. Using Equation 30, we find that the ratio of free-free to electron scattering opacity along a solution is given by

$$\frac{\tilde{\kappa}_{\beta=0}^{(F)}}{\tilde{\kappa}_{\beta=0}^{(T)}} = 1.74 \times 10^6 \rho_0^{-5/9} \left(\frac{\beta}{\sqrt{\ln b_{\text{Typical}}}} \right)^{14/9} A_{56}^{4/3} Z_{26}^{-10/9} T_{\text{eff},6}^{-28/9} g_{s,14}^{7/9}, \quad (34)$$

where the electron scattering opacity $\tilde{\kappa}_{\beta=0}^{(T)}$ is given by Silant'ev & Yakovlev (1980). Since this ratio increases with decreasing density, we only need to estimate it at the maximum density for the solution, *i.e.* the density at the onset of degeneracy

$$\left. \frac{\tilde{\kappa}_{\beta=0}^{(F)}}{\tilde{\kappa}_{\beta=0}^{(T)}} \right|_{\text{ND/D}} = 1.36 \times 10^3 \beta (\ln b_{\text{Typical}})^{-6/7} A_{56}^{6/7} Z_{26}^{-5/7} T_{\text{eff},6}^{-24/7} g_{s,14}^{6/7}. \quad (35)$$

For $B = 10^{14}$ G this ratio is greater than one for $T_{\text{eff}} < 5.9 \times 10^6$ K, which is larger than the effective temperatures considered here. Furthermore, this is a conservative estimate of this ratio because generally we cut off the nondegenerate solution where degenerate electrons begin to dominate the heat conduction. In unmagnetized envelopes this occurs where the gas is mildly degenerate (Hernquist & Applegate 1984). We find that this is also the case for strongly magnetized envelopes.

5 Calculations

5.1 Strategy

We have found that the heat transfer equation is not solvable analytically, but it is separable in several cases. For the liquid and degenerate region of the envelope the solution may be calculated once for each field strength and geometry, and scaled to reflect the magnitude of the heat flux and shifted to fit the temperature at the low density edge of the region. We can apply this same strategy in the solid state only for the case of a purely radial or azimuthal field. Otherwise, for the solid region, the temperature as a function of chemical potential will depend on the flux and boundary conditions in a more complicated way; consequently, the solution must be recalculated for each value of the flux. To match the solutions across the liquid-solid phase transition and the degenerate-nondegenerate interface, we follow the approach of Hernquist & Applegate (1984). At the outer boundary, we use the radiative zero solution.

5.2 Results for the separable structure equations

As described earlier, in the low-temperature limit when only one Landau level is filled the structure equation is simple and may be integrated for a given field strength and geometry and the boundary conditions and the dependence on the flux may be satisfied after the numerical solution is obtained.

Given these numerical results, it is straightforward to calculate the core temperature for a given surface temperature and flux. However, before fixing the boundary conditions, we can note several general features of the results. First, for transport along the magnetic field, the envelope becomes nearly isothermal at $\zeta - 1 \sim 0.1$ regardless of the magnetic field strength. However, for transport perpendicular to the field, the temperature rises steadily throughout the range of applicability of this formalism.

Parallel Transport In Figure 1 we present results for the degenerate and non-degenerate regime for several magnetic fields with an effective surface temperature of 10^6 K. In the nondegenerate regime the temperature solution follows the power-law given in Equation 30 and the *conductivity* is nearly constant. In the degenerate regime, the conductivity increases dramatically and the *temperature* remains nearly constant. For the solution with $B = 10^{15}$ G, the discontinuity in the conductivity at the phase transition is apparent. The results for 10^{14} G qualitatively agree with the results of Hernquist (1985) for this field strength. Quantitatively however, we find that the conductivity in the nondegenerate regime is thirty percent lower than the earlier result of 10^{14} erg/(K cm s) and is given by Equation 29. As the magnetic field strength increases, we find that the core temperature (or here the temperature at which the first Landau level is filled) decreases. This effect results from the increased conductivity in

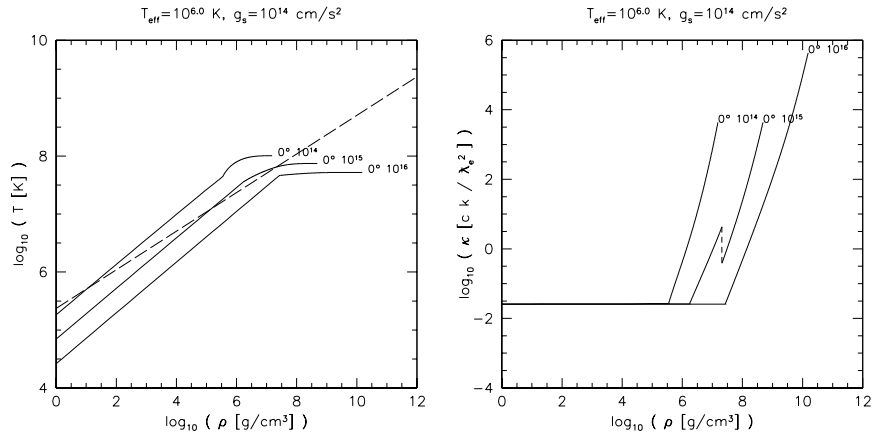


Figure 1: Thermal structure of a strongly magnetized neutron star envelope for a radial field. The left panel traces the temperature-density relation with $B = 10^{14}, 10^{15}, 10^{16} \text{ G}$ and effective surface temperature of 10^6 K . The right panel traces the conductivity through the envelope. The constant conductivity solution appropriate for a purely power-law conductivity law works well through the nondegenerate regime. In the left panel, liquid phase exists above the dashed curve, and solid phase exists below.

the nondegenerate regime where κ is approximately proportional to β^2 and the degenerate regime where the quantization of the electron phase space increases the conductivity above the zero-field values.

We take advantage of the simplicity of this analytic technique when calculating the thermal structure for hotter and cooler surface temperatures. We do not need to reintegrate the structure equations themselves. All that is required is to recalculate the boundary conditions at the non-degenerate-degenerate interface and the liquid-solid phase transition. Again we find qualitative agreement with Hernquist (1985). In the nondegenerate regime, the increased or decreased flux mimics the effect of changing the field strength depicted in Figure 1.

We compare the various results by determining the temperature at the following densities: $\rho = 1.5 \times 10^7$, 4.7×10^8 and 1.5×10^{10} g/cm³. These are the densities at which the lowest Landau level fills for field strengths of 10^{14} , 10^{15} and 10^{16} G. Moreover, since the matter is nearly isothermal at higher densities, these temperatures are close to the core temperature, at least for parallel transport. By fitting the results of the calculations, we find that at the lowest density:

$$T(\rho = 1.5 \times 10^7 \text{ g/cm}^3) \propto \beta^{-0.19} \left(\frac{F}{g_s} \right)^{0.35} \quad (36)$$

and at both the higher densities

$$T(\rho = 4.7 \times 10^8 \text{ g/cm}^3, 1.5 \times 10^{10} \text{ g/cm}^3) \propto \beta^{-0.16} \left(\frac{F}{g_s} \right)^{0.43}. \quad (37)$$

Figure 2 compares the numerical results with the best-fit power-law relations.

Perpendicular Transport Modeling the transition between photon and electron heat transport is qualitatively different for transport perpendicular to the field lines. In the parallel case, the conductivity from electrons typically increases rapidly with density, and the transition from photon to electron-dominated heat transport is abrupt. For perpendicular transport, the function Q decreases with energy, and therefore the conductivity decreases with density for fixed temperature. In this case the transition is more subtle. Fortunately, the solution does not depend strongly on how this transition is treated, so we choose to employ $\zeta - 1 > \tau$ to delineate the region where electron conduction dominates. The conductivity is not continuous across this transition as is apparent in Figure 3.

We varied the definition of the non-degenerate-degenerate interface and found that it had little effect on the $T_{\text{max}} - T_{\text{eff}}$ relation. Figure 4 shows how the solution changes if we move the interface to a factor of ten higher or lower temperature (*i.e.* $\zeta - 1 > 10\tau$ and $\zeta - 1 > \tau/10$). Although near the interface the solutions differ dramatically, at higher densities the choice has little effect. The boundary condition at the transition is unimportant for perpendicular transport, because the temperature rises quickly with density, and the

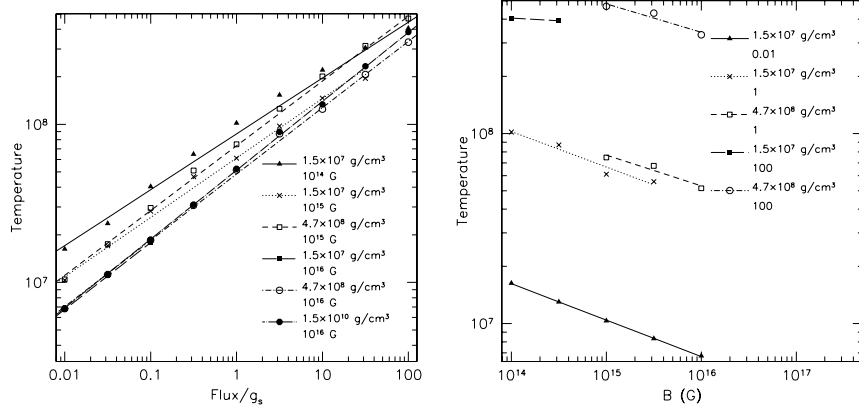


Figure 2: The left panel depicts the temperature-flux relation for several field strengths and densities. F/g_s is given in units of $\sigma(10^6 K)^4/10^{14}$ cm/s². The right panel depicts the temperature-magnetic-field relation. The symbols show the calculated data points and the lines are the best-fit power law functions to the data.

solution quickly “forgets” the boundary conditions, in a manner analogous to the convergence of the radiative zero solution to the true solution in stellar atmospheres (*e.g.* Schwarzschild 1965). This is in contrast to the case where $\psi \neq \pi/2$ where the material quickly becomes isothermal in the degenerate regime.

We find that for a given effective temperature the core temperature is much higher where the heat must travel perpendicularly to the field lines. Furthermore, we find that for stronger field strengths the effect is more pronounced.

Effective Temperature Distributions To find the effective temperature as a function of angle with respect to the magnetic field we vary the effective temperature as a function of angle until the temperature where the first Landau level fills is constant for the various angles. Unfortunately, where the magnetic field is neither radial or tangential we have solutions only in the non-degenerate and liquid degenerate regimes. Therefore, for acute angles we must select fluxes such that the degenerate solution is entirely in the liquid regime. For the more strongly magnetized envelopes we can follow the solution to higher densities; consequently, we must use larger effective temperatures for the stronger magnetic fields. Table 2 summarizes the parameters for the calculations. Figure 5 depicts the results for $B = 10^{14}$ and 10^{16} G. For all but the perpendicular case, the envelope has become nearly isothermal by the density where the first Landau level fills.

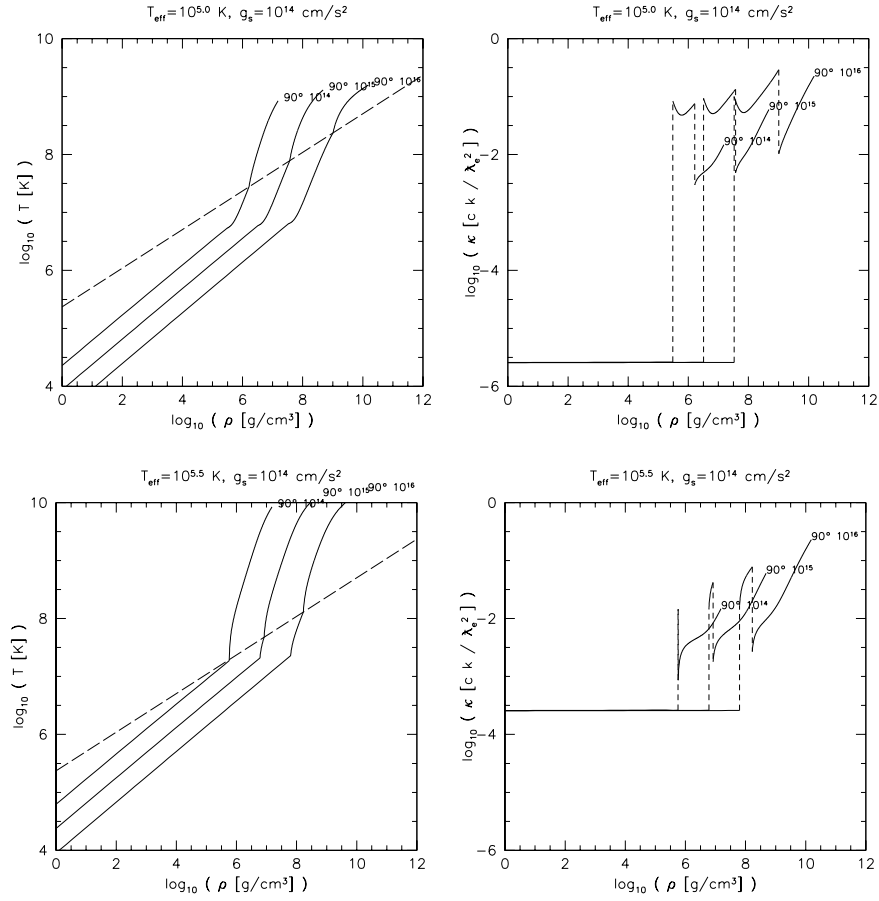


Figure 3: Same as Figure 1 for the perpendicular case.

Table 2: Results of the Two Dimensional Calculations

Field Strength [G]	$T_{\text{eff}}(\psi = 0)$ [K]	$T_{\text{max}}(\zeta = \sqrt{2\beta + 1})$ [K]
10^{14}	1.07×10^6	1.12×10^8
10^{15}	3.16×10^6	4.79×10^8
10^{16}	5.06×10^6	8.13×10^8

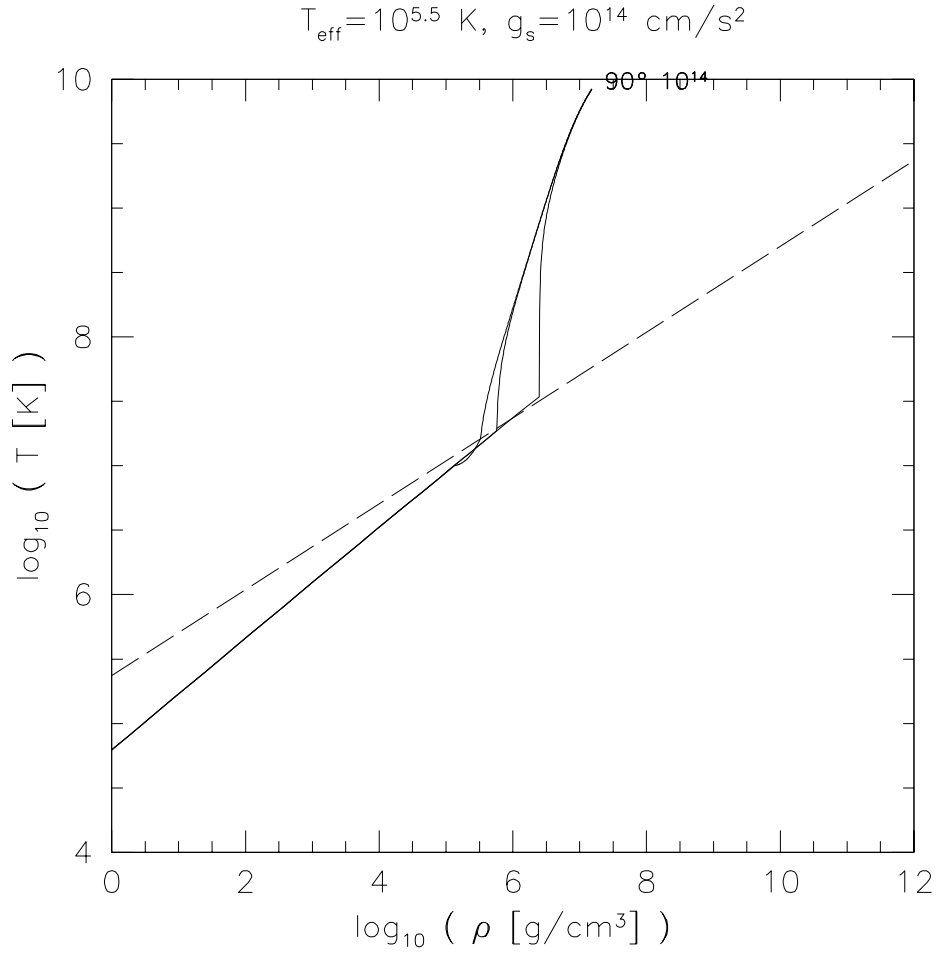


Figure 4: The dependence of the envelope solution for transport perpendicular to the magnetic field upon the definition of the non-degenerate-degenerate interface. We have calculated the location of the interface for $(\zeta - 1)/\tau = 0.1, 1, 10$ from left to right.

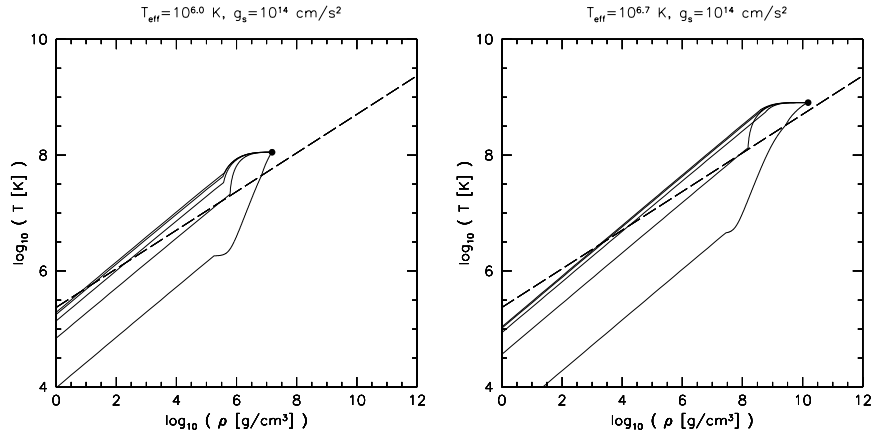


Figure 5: The left panel shows the temperature structure of the envelope as a function of density for $B = 10^{14}$ G and $T_{\text{eff}} = 1.07 \times 10^6$ K. From top to bottom, the results are for $\psi = 0^\circ, 30^\circ, 60^\circ, 85^\circ, 90^\circ$ where ψ is the angle between the magnetic field and the radial direction. The right panel depicts the temperature structure for $B = 10^{16}$ G and $T_{\text{eff}} = 5.06 \times 10^6$ K. The solutions are constrained to have the same temperature at the density where the first Landau level fills (denoted by the bold circle). In both panels, liquid phase exists above the dashed curve, and solid phase exists below.

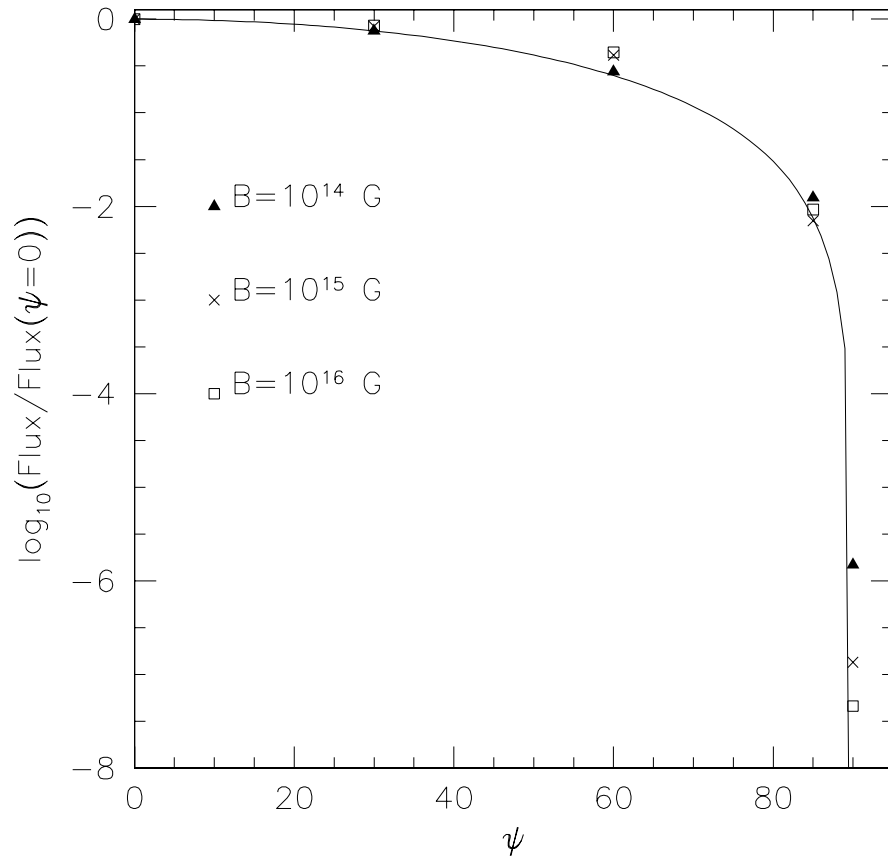


Figure 6: Flux as a function of angle for $B = 10^{14}, 10^{15}$ and 10^{16} G. The solid curve is $\cos^2 \psi$.

Figure 6 shows the flux as a function of angle for all of the two-dimensional calculations. The agreement between the flux distribution and a simple $\cos^2 \psi$ law is striking. Greenstein & Hartke (1983) have argued that if the conductivity is constant through the envelope, the flux will follow a distribution of the form $A \cos^2 \psi + B \sin^2 \psi$. Although in the nondegenerate regime the conductivity along a $T(\rho)$ solution is nearly constant, in the degenerate regime it varies by several orders of magnitude. Furthermore, the nondegenerate layers do not throttle the heat flux; if they did, one would expect little variability, as the conductivity parallel and perpendicular to the field are nearly equal in the strong field limit.

We look to the degenerate structure equation for the liquid state to explain the remarkable agreement with a $\cos^2 \psi$ distribution. From examination of Equation 18, we see that if the conductivity transverse to the field is neglected, we can make the replacement

$$F \rightarrow F \cos^2 \psi \quad (38)$$

and recover the thermal structure equation for $\psi = 0$. We determine where this approximation is valid by comparing the transverse and parallel components of the conductivity tensor

$$\frac{\kappa_{yy,ei}}{\kappa_{zz,ei}} = \frac{Z^2 \alpha^4}{4\pi^2 \beta^3} (\zeta^2 - 1) \frac{Q_{ei}(\zeta; \beta)}{\phi_{ei}(\zeta; \beta)} = 8.22 \times 10^{-11} \frac{Z_{26}^4}{A_{56}^2 B_{14}^5} \rho_6^2 \frac{Q_{ei}(\zeta; \beta)}{\phi_{ei}(\zeta; \beta)}. \quad (39)$$

At first glance, it appears that the transverse conductivity is negligible throughout the degenerate regime. However, the functions Q_{ei} and ϕ_{ei} complicate the discussion. Specifically, $\phi_{ei} \rightarrow 0$ and $Q_{ei} \rightarrow \infty$ as $\zeta \rightarrow 1$; therefore, transverse conduction is likely to be important in the nonrelativistic portion of the degenerate envelope. Figure 5 shows that this is indeed the case. For $B = 10^{14}$ G, the solutions for $\psi < \pi/2$ are nearly identical for $\rho > 10^{6.5}$ g/cm³ or $\zeta > 1.1$. As ζ approaches unity, the ratio of the conductivities increases without bound, the transverse conductivity may no longer be neglected, and the runs of temperature with density begin to diverge.

Empirically, we find that in the region of the envelope which most effectively throttles the flux, the transverse conductivity may be neglected for $\psi < \pi/2$ without introducing significant error.

5.3 Observed Flux Distribution

We follow the technique outlined by Page (1995) to calculate the observed fluxes. However, unlike Page (1995) we evaluate the double integrals over the visible portion of the neutron star surface directly. We use the $\cos^2 \psi$ rule to calculate the photon distribution function at the surface, and so we do not define a grid of precalculated distribution functions as Page (1995) does.

As a first approximation, we focus on the variation of the observed bolometric flux with the angle φ of the line of sight with the magnetic dipole axis. This angle is a function of the phase angle (γ), the inclination of the dipole to the rotation axis (α) and the line of sight to the rotation axis (ζ)

$$\cos \varphi = \cos \zeta \cos \alpha + \sin \zeta \sin \alpha \cos \gamma \quad (40)$$

(Greenstein & Hartke 1983). For simplicity, in the discussion that follows we will take $\alpha = \zeta = \pi/2$; therefore $\varphi = \gamma$ and we refer to $\varphi = 0, \pi$ as on-phase and $\varphi = \pi/2, 3\pi/2$ as off-phase.

We repeat the calculation for several values of the stellar radius (with fixed mass) to determine the effects of general relativity on the light curves: gravitational redshift and the deflection of null geodesics (self-lensing, or more concisely “lensing”).

To quantify the effect of gravitational lensing on the light curves of magnetized neutron stars, we calculate the mean value of the bolometric flux emitted by the surface over the visible region of the star. We assume that the flux at a given location on the surface is proportional to $\cos^2 \psi$ where ψ is the angle between the radial direction and the magnetic field.

For clarity, we treat the gravitational redshift separately. Figure 7 depicts the ratio of the mean value of the flux over the visible portion of the star to the flux that would be emitted if the magnetic field were normal to the surface throughout (*i.e.* an isotropic temperature distribution).

In the limit of infinite radius, *i.e.* if lensing is unimportant, we find that for a uniform field

$$\bar{f}(\varphi = 0) = \frac{1}{2}f(\psi = 0) \text{ and } \bar{f}(\varphi = \pi/2) = \frac{1}{4}f(\psi = 0). \quad (41)$$

For a dipole field, the calculation is slightly more complicated. First, we used Equation 10 to determine the angle of the field with respect to the radial direction. Secondly from equations 36 and 37, we find that the emergent flux is a function of the field strength. For a dipole configuration, the magnitude of the field varies as

$$\beta \propto \sqrt{3 \cos^2 \theta + 1} \quad (42)$$

along the surface of the star. Since we are most interested in fixing the internal temperature at high densities we assume that the flux is proportional to $B^{0.4}$ from Equation 37 which reduces the flux for $\theta \sim \pi/2$ further beyond the $\cos^2 \psi$ rule. We obtain

$$\bar{f}(\varphi = 0) = 0.663f(\psi = 0) \text{ and } \bar{f}(\varphi = \pi/2) = 0.393f(\psi = 0). \quad (43)$$

If we did not include the effect that the flux is a function of field strength as well as orientation we would have obtained 0.717 and 0.444 for the above values.

We find that the mean flux is greater for the dipole configuration than for a uniform field for all viewing angles if $R/R_s < 5$, and that the variation in

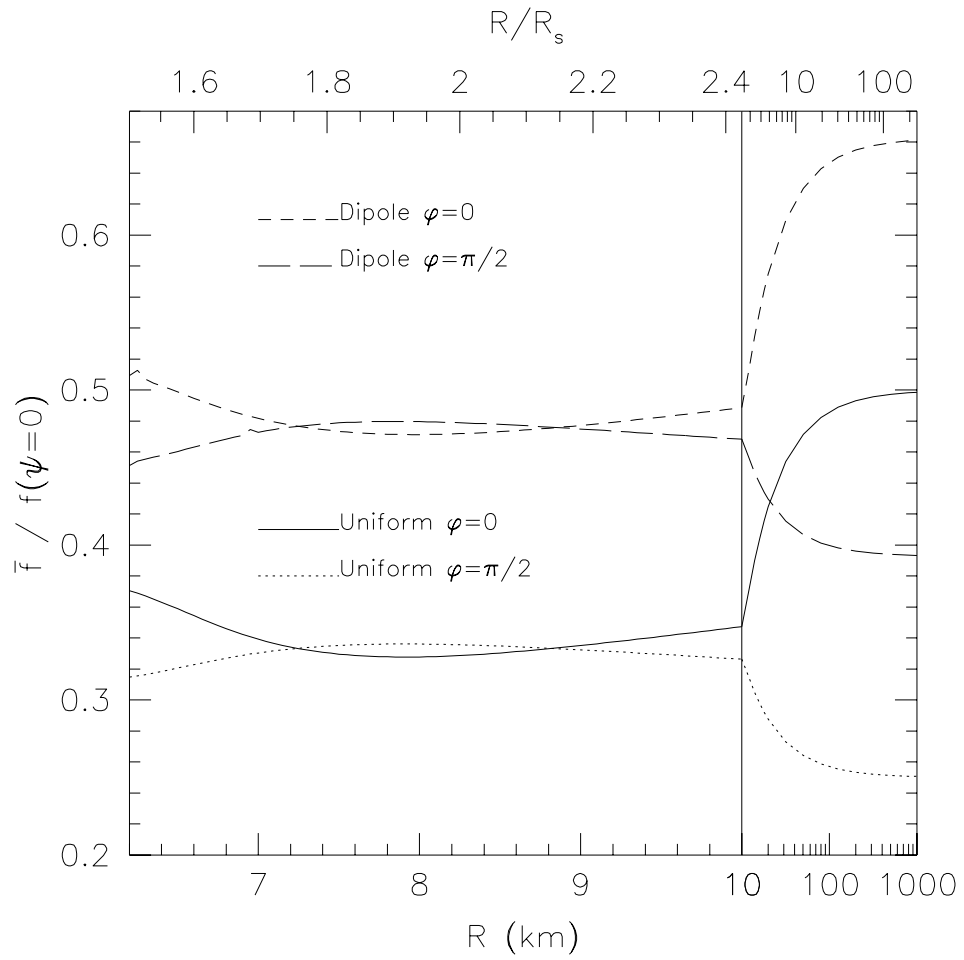


Figure 7: The average of the bolometric flux over the visible portion of the neutron star for $\varphi = 0, \pi/2$. The upper pair is for a dipole, and the lower is a uniform field configuration.

the light curve is generally smaller. We have taken $M_{\text{NS}} = 1.4M_{\odot}$, yielding a Schwarzschild radius, R_s , of 4.125 km. The theoretical predictions for the radius of a $1.4M_{\odot}$ neutron star range from 6.5 km to 14 km (Thorsson, Prakash & Latimer 1994; Pandharipande 1971; Wiringa, Fiks & Fabrocini 1988), depending on the details of the equation of state at supernuclear densities.

As Page (1995) found, lensing dramatically reduces the variation of the observed flux with phase by making more than half the surface visible at any time. Interestingly, for the range of radii 7.248 – 8.853 km, we find that the flux is greater when the magnetic poles are located perpendicular to the line of sight. For this range of radii over 90% of the surface is visible. Emission from both of the hotspots reaches the observer leading to a larger flux. For radii less than 7.248 km the entire surface is visible and again the peaks are on phase. Page (1995) found a similar effect for the same range of radii.

The emitted spectra from the visible portion of the neutron-star surface is the sum of blackbody spectra of various temperatures. To determine the emitted spectra, we calculate the distribution of blackbody temperatures on the surface; *i.e.* we estimate the distribution function $d\bar{f}/dT_{\text{eff}}$. With this distribution function, it is straightforward to calculate the emergent spectrum averaged over the visible portion of the surface as

$$\bar{f}_{\omega} = \int_0^{\infty} \frac{d\bar{f}}{dT_{\text{eff}}} \frac{1}{\sigma T_{\text{eff}}^4} \frac{\hbar}{4\pi^2 c^2} \frac{\omega^3}{\exp(\hbar\omega/kT) - 1} dT_{\text{eff}}. \quad (44)$$

The factor of σT_{eff}^4 converts the flux to an effective area of emission (\bar{A}). The calculation of $d\bar{f}/dT_{\text{eff}}$ is numerically more tractable than $d\bar{A}/dT_{\text{eff}}$ and allows us to account for the total energy emitted more reliably.

We calculate $d\bar{f}/dT_{\text{eff}}$ in similar fashion to \bar{f} . To expedite the calculation, we note that given the $\cos^2 \psi$ rule the neutron star surface has a limited range of effective temperatures, specifically between 0 and $T_{\text{eff}}(\psi = 0)$. Consequently we define

$$\tilde{T} = \frac{T_{\text{eff}}}{T_{\text{eff}}(\psi = 0)} \quad (45)$$

$$\frac{d\bar{f}}{d\tilde{T}} = \frac{d\bar{f}}{dT_{\text{eff}}} T_{\text{eff}}(\psi = 0). \quad (46)$$

For observations on-phase ($\varphi = 0$) and without lensing ($R \rightarrow \infty$), the flux-weighted temperature distribution can be calculated directly if the envelope is uniformly magnetized. It is given by

$$\frac{d\bar{f}}{d\tilde{T}} = 4\tilde{T}^{\gamma} f(\psi = 0). \quad (47)$$

The result for the dipole cannot be written explicitly and is not illustrative.

For a general geometry ($\varphi \neq 0$), we expand this function in an orthonormal basis on the interval 0 to 1. Specifically, we assume that for $0 \leq \tilde{T} \leq 1$

$$\frac{d\bar{f}}{d\tilde{T}} = \sum_{l=0}^{\infty} A_l Q_l(\tilde{T}) \quad (48)$$

and zero otherwise, where

$$Q_l(\tilde{T}) = \sqrt{2l+1} P_l(2\tilde{T} - 1). \quad (49)$$

The $P_l(x)$ are the Legendre polynomials. From the properties of these orthonormal functions, we have $A_0 = \bar{f}$, and A_l is calculated by inserting the weighting function $Q_l(\tilde{T})$ into the integrands in the calculation for \bar{f} . We recall that we have assumed, $\tilde{T} = \cos^{1/2} \psi$

Using an orthonormal basis dramatically speeds the calculation of the distribution. Additionally, because the $P_l(x)$ are polynomials, it is straightforward to calculate conventional statistics of the distribution

$$\langle \tilde{T} \rangle = \frac{1}{\bar{f}} \int_0^1 \tilde{T} \frac{d\bar{f}}{d\tilde{T}} d\tilde{T} = \frac{\sqrt{3}}{6} \frac{A_1}{A_0} + \frac{1}{2} \quad (50)$$

$$\langle \tilde{T}^2 \rangle = \frac{\sqrt{5}}{30} \frac{A_2}{A_0} + \frac{\sqrt{3}}{6} \frac{A_1}{A_0} + \frac{1}{3}. \quad (51)$$

Unfortunately, with this basis is impossible to insist that distribution is everywhere non-negative, *i.e.* that no temperatures contribute negative flux. However, if a sufficiently large number of A_l are calculated, the intervals where $d\bar{f}/d\tilde{T} < 0$ can be made to be arbitrarily small and to have an arbitrarily small contribution to the total flux. We compare the results of the expansion with Equation 47 and find that the maximum relative error in the expansion coefficients between the two techniques is approximately 9×10^{-5} .

Figure 8 depicts the results of this calculation for four values of the stellar radius with $\varphi = 0, \pi/2$. In the left panel, we see in the absence of general relativistic effects that when the neutron star is off-phase more flux is produced at lower blackbody temperatures than when the magnetic dipole is pointing toward the observer. For the smallest radius considered ($R = 6.25$ km), the entire surface of the neutron star is visible and a large portion of the front hemisphere has a second image. In this case, both the flux-weighted temperature distributions at $\varphi = 0$ and $\pi/2$ are peaked at the maximum effective temperature. However, the distribution off-phase has a more well populated tail extending toward lower temperatures than on-phase.

The right panel depicts a value of the stellar radius ($R = 8.85$ km) where there is practically no variation of \bar{f} with phase. Additionally, we see that the flux-weighted temperature distributions are nearly constant with phase. Also depicted is the temperature distributions for $R = 7.9$ km, the radius where the

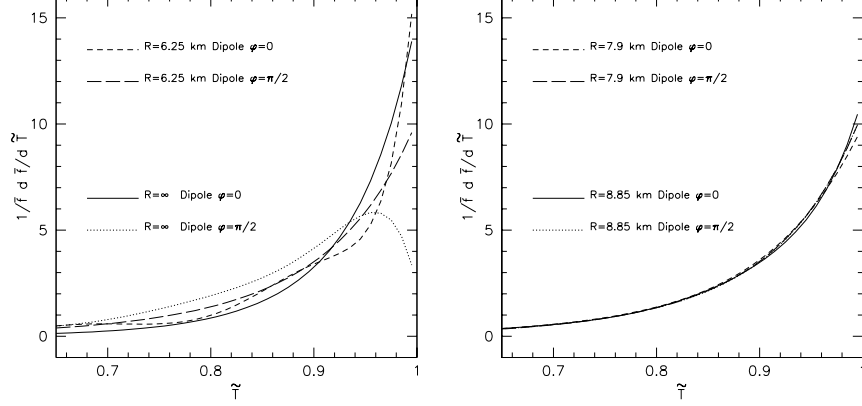


Figure 8: The fractional distribution of observed flux as function of the surface blackbody temperature. The left panel depicts the distribution for the minimal ($R/R_s = 1.52$) and maximal radii ($R = \infty$) considered. The right panel depicts the distribution at a radii where $\bar{f}(\varphi = 0) = \bar{f}(\varphi = \pi/2)$ ($R = 8.85$ km) and where the off-phase peaks are maximized ($R = 7.9$ km). All the curves are normalized to have an integral of unity from $\tilde{T} = 0$ to 1

off-phase peaks are maximized. Here again, the distributions do not change appreciably with phase. We conclude that for $7 \lesssim R \lesssim 9$ km, it would be difficult to detect variation of the spectra with phase, if the neutron star surface indeed radiates as a blackbody.

To calculate the spectra themselves, it is convenient to define the following functions,

$$\mathcal{F}_l(\tilde{\omega}) = \frac{15}{\pi^4} \tilde{\omega}^3 \int_0^1 Q_l(\tilde{T}) \frac{1}{\tilde{T}^4} \frac{1}{\exp(\tilde{\omega}/\tilde{T}) - 1} d\tilde{T}, \quad (52)$$

where $\tilde{\omega} = \hbar\omega/kT_{\text{eff}}(\psi = 0)$, so that

$$\bar{f}_\omega(\omega) = \frac{\hbar}{kT_{\text{eff}}(\psi = 0)} \sum_{l=0}^{\infty} A_l \mathcal{F}_l \left(\frac{\hbar\omega}{kT_{\text{eff}}(\psi = 0)} \right). \quad (53)$$

Since A_l has units of flux, we obtain the correct units of flux-time for \bar{f}_ω .

To convert to the observed spectra, we must account for gravitational redshift and interstellar absorption; we obtain (Page 1995)

$$f_\omega^{\text{observed}}(\omega) = \bar{f}_\omega(e^{-\Lambda_s} \omega) e^{-\Lambda_s} \frac{R_\infty^2}{D^2} e^{-N_H \sigma(\omega)} \quad (54)$$

where

$$R_\infty \equiv R e^{\Lambda_s} \quad (55)$$

where $e^{-\Lambda_s}$ is given in Equation 6. The final term accounts for interstellar absorption and D is the distance to the neutron star. For $\sigma(E)$ we use the Morrison & McCammon (1983) cross-sections.

Figure 9 depicts the spectra in the ROSAT energy range for two neutron stars. Each of the spectra (light curves) is well fitted by a blackbody (heavy curves) at the mean effective temperature with an additional hard component. The mean effective temperature (T_{mean}) is defined by

$$\int f_{\omega}^{\text{observed}}(\omega) d\omega = \sigma T_{\text{mean}}^4 \frac{R_{\infty}^2}{D^2} \quad (56)$$

for $N_H = 0$, *i.e.* it is the equivalent blackbody temperature that accounts for all of the energy emitted from the neutron star surface. The hard component is most significant when the star is observed at right angles to the magnetic axis, and originates from the portions of the hot polar caps that are visible even when the star is off-phase.

In Appendix A, we present two XSPEC models which are available over the WWW. With these models, one may simulate observations from various x-ray instruments to estimate the observed pulsed fractions for the models discussed in this section. We give an example in Figure 11.

5.4 Neutron Star Cooling

We can use the results of the preceding sections to determine the effects of the magnetic field on neutron star cooling rates. Specifically, we take the ratio of the total flux from the surface with and without a magnetic field for the same core temperature. We have used the results of Hernquist & Applegate (1984). To determine the core temperature for a given flux we combine their equations (4.7) and (4.8), switching from the first relation to the second when the surface effective temperature drops below 4.25×10^5 K. The results do not depend qualitatively on whether equation (4.7) or (4.8) of Hernquist & Applegate (1984) is used.

To compare our calculated temperature-flux relation with the results for isotropic heat transport, we multiply the fluxes for the magnetized envelopes by 0.4765 to account for a dipole field configuration. Additionally, we assume in our calculations that the envelope is isothermal above the density (ρ_{max}) at which the first Landau level fills and use the temperature (T_{max}) at this density to estimate the flux in the unmagnetized case. Only for the strongest field strength considered ($B = 10^{16}$ G) do our analytic calculations extend to the core density assumed by Hernquist & Applegate (1984) of 10^{10} g/cm³; however, we do not expect the results to be strongly sensitive to this cutoff density as our solutions (for $\psi \neq \pi/2$) are nearly isothermal at high densities.

Figure 10 depicts the results of this comparison. We find that for the weakest field strength considered ($B = 10^{14}$ G), the magnetic field has little effect on the

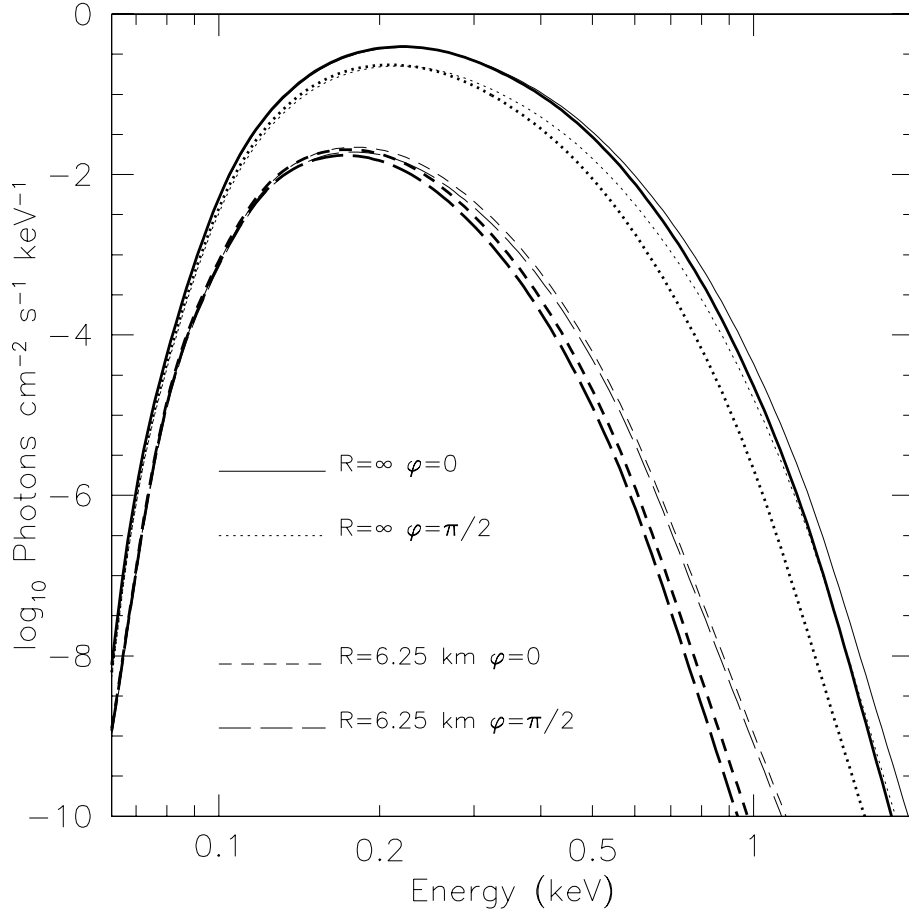


Figure 9: The observed spectra from a neutron star with $T_{\text{eff}}(\psi = 0) = 7.5 \times 10^5$ K from a distance of 250 pc with an intervening absorption column of $N_H = 10^{20} \text{cm}^{-2}$. The light curves show the spectra, and the heavy curves show blackbody spectra at the mean effective temperature of the neutron star. For the $R = \infty$ model, we have taken $R/R_s \rightarrow \infty$ while $R = 20$ km to give the surface area of the neutron star, while neglecting general relativistic effects.

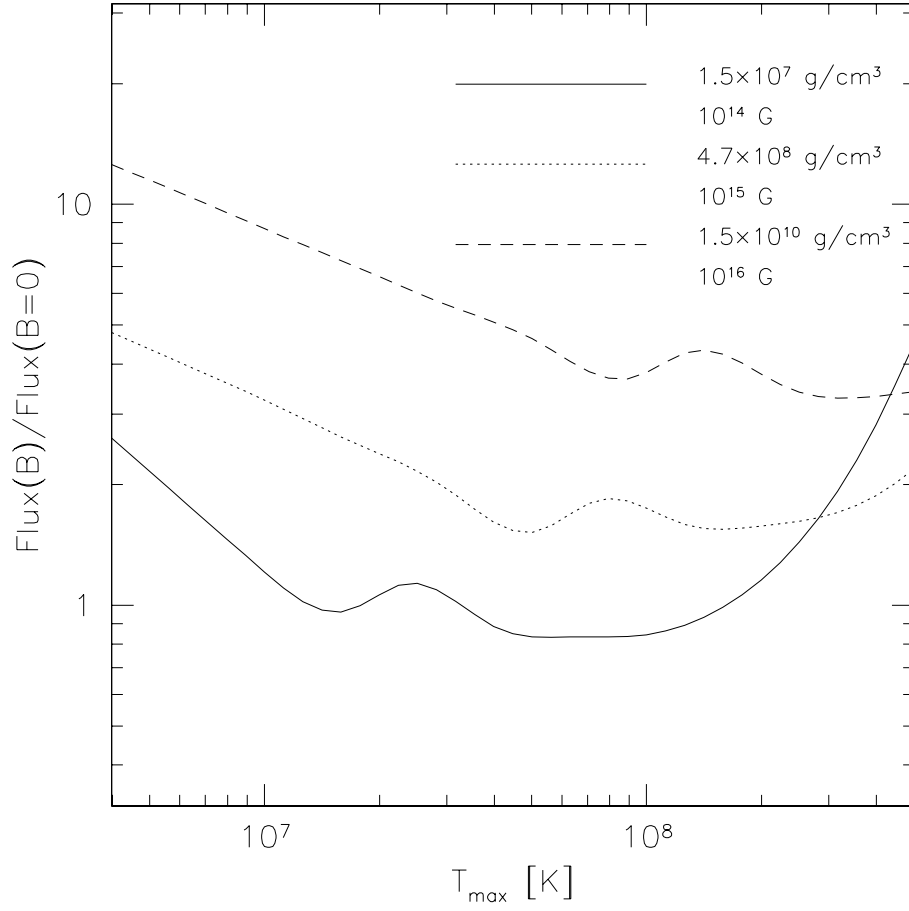


Figure 10: The ratio of fluxes in magnetized envelopes to those in unmagnetized ones. We have assumed that the envelope is isothermal above the densities given in the legend to estimate the unmagnetized fluxes.

total luminosity of the star. However, for cooler core temperatures and stronger magnetic fields, the difference in the luminosities can be up to a factor of ten. The flux ratio is sensitive to the core temperature because Equations 36 and 37 have a slightly different power-law index than the model assumed for the unmagnetized envelope (0.392). The inflection in each of the curves occurs when the material near non-degenerate-degenerate interface melts as the core temperature increases. All the curves swing upward for high values of T_{\max} because for high fluxes (*i.e.* high core temperatures) our assumption that the temperature is constant for $\rho > \rho_{\max}$ no longer holds.

Because strongly magnetized neutron stars emit significantly more flux, we expect that the thermal history of magnetars should be dramatically different from that of neutron stars with weaker magnetic fields. We discuss this issue further in Heyl & Hernquist (1997).

6 Conclusions

We have presented an analytic technique for calculating the thermal structure of ultramagnetized neutron star envelopes. We use the exact thermal conductivities in an intense magnetic field of Silant'ev & Yakovlev (1980) and Hernquist (1984) in the non-degenerate and degenerate regimes, respectively. We make two simplifying approximations. We assume that the interface between degenerate and non-degenerate material is abrupt. Hernquist (1985) numerically calculated the thermal structure for $B = 10^{14}$ G without this assumption. Our agreement with this earlier result shows that an abrupt interface is a good approximation. Secondly, we use a standard simplification in the study of stellar atmospheres which is to use the radiative zero solution to fix the outer boundary condition (Schwarzschild 1965). Because the equation for the thermal structure in the outermost layers is qualitatively similar to the relation for an unmagnetized envelope, we conclude that as in the unmagnetized case (Hernquist & Applegate 1984), this is also an accurate approximation.

A distinct approach is to treat the entire problem numerically, which allows us to estimate directly the possible errors that our simplifying assumptions introduce and alleviates the problem of how to treat the regions where more than one Landau level is filled. Numerical models for parallel and transverse conduction for $B = 10^{12} - 10^{14}$ G and $\rho < 10^{10}$ g/cm⁻³ are presented in Heyl & Hernquist (1998).

We find that the relation between transmitted flux, core temperature and field strength may be approximated by a power law and that the effective temperature is proportional to $\cos^{1/2} \psi$ where ψ is the angle between the radial direction and the local direction of the magnetic field. Using the geometric result, we calculate the observed spectra as a function of viewing angle including the effects of general relativity for dipole and uniform field configurations. We extend the conclusions of previous work. If the surface is assumed to radiate as a

blackbody and neutron stars have radii within the currently accepted range, the anisotropic heat transport induced by a dipole field configuration is insufficient to produce the observed pulsed fractions even for ultramagnetized envelopes.

Pavlov et al. (1994) argue that in addition to the transmission of heat through the envelope, the emission at the surface is also strongly anisotropic. Anisotropic emission can naturally produce large pulsed fractions even when the temperature on the surface is uniform (Zavlin et al. 1995, Shibano et al. 1995). Additionally, the composition of the atmosphere may have a profound effect on the emergent radiation. A magnetized iron atmosphere produces substantial limb darkening for $\psi \sim \pi/2$, and the decrement is strongest at high energies (Rajagopal, Romani & Miller 1997). It is straightforward to graft these atmospheres onto the thermal envelopes calculated here to obtain the observed time-dependent spectra for a variety of realistic neutron star models. These effects along with anisotropic conduction may be sufficient to account for the large observed pulsed fractions.

Acknowledgements

We would like to thank the referee, Vadim Urpin, for valuable suggestions. This work was supported in part by a National Science Foundation Graduate Research Fellowship, the NSF Presidential Faculty Fellows program and Cal Space grant CS-12-97.

Bibliography

- Anderson, S. B., Córdoba, F. A., Robinson, G. G. P. C. R. & Thompson, Jr., R. J. 1993, *ApJ*, **414**, 867.
- Becker, W. & Trümper, J. 1993, *Nature*, **365**, 528.
- Blandford, R. D. & Hernquist, L. 1982, *J. Phys. C: Solid State Phys.*, **15**, 6233.
- Cox, J. P. & Giuli, R. T. 1968, *Principles of Stellar Structure*, Gordon and Breach, New York
- Finley, J., Ögelman, H. & Kiziloglu, Y. 1992, *ApJL*, **394**, 21.
- Glen, G. & Sutherland, P. 1980, *ApJ*, **239**, 671.
- Greenstein, G. & Hartke, G. J. 1983, *ApJ*, **271**, 283.
- Greiveldinger, C. et al. 1996, *ApJL*, **465**, 35.
- Gudmundsson, E. H., Pethick, C. J. & Epstein, R. I. 1982, *ApJL*, **259**, 19.
- Halpern, J. P. & Holt, S. S. 1992, *Nature*, **357**, 222.

- Halpern, J. P. & Ruderman, M. 1993, *ApJ*, **415**, 286.
- Halpern, J. P. & Wang, F. Y. H. 1997, *ApJ*, **477**, 905.
- Hernquist, L. 1984, *ApJS*, **56**, 325.
- Hernquist, L. 1985, *MNRAS*, **213**, 313.
- Hernquist, L. & Applegate, J. H. 1984, *ApJ*, **287**, 244.
- Heyl, J. S. 1998, *Ph.D. thesis*, University of California at Santa Cruz
- Heyl, J. S. & Hernquist, L. 1997, *ApJL*, **491**, 95.
- Heyl, J. S. & Hernquist, L. 1998, *MNRAS*, submitted
- Morrison, R. & McCammon, D. 1983, *ApJ*, **270**, 119.
- Nomoto, K. & Tsuruta, S. 1981, *ApJL*, **250**, 19.
- Ögelman, H. 1995, in M. A. Alpar, U. Kiziloglu & J. V. Paradijs (eds.), *The Lives of Neutron Stars*, p. 101, Kluwer, Dordrecht
- Ögelman, H. & Finley, J. P. 1993, *ApJL*, **413**, 31.
- Ögelman, H., Finley, J. P. & Zuckerman, H. U. 1993, *Nature*, **361**, 136.
- Page, D. 1995, *ApJ*, **442**, 273.
- Pandharipande, V. R. 1971, *Nucl Phys A*, **178**, 178.
- Pavlov, G. G., Shibano, Y. A., Ventura, J. & Zavlin, V. E. 1994, *A&A*, **289**, 837.
- Pavlov, G. G. & Yakovlev, D. G. 1977, *Astrophysics*, **13**, 89.
- Possenti, A., Mereghetti, S. & Colpi, M. 1996, *A&A*, **313**, 565.
- Potekhin, A. Y. & Yakovlev, D. G. 1996, *A & A*, **314**, 341.
- Rajagopal, M., Romani, R. W. & Miller, M. C. 1997, *ApJ*, **479**, 347.
- Schaaf, M. E. 1988, *A&A*, **205**, 335.
- Schaaf, M. E. 1990, *A&A*, **227**, 61.
- Schwarzschild, M. 1965, *Structure and Evolution of the Stars*, Dover, New York
- Shibano, Y. A., Pavlov, G. G., Zavlin, V. E. & Tsuruta, S. 1995, in H. Böhringer, G. E. Morfill & J. E. Trümper (eds.), *Seventeenth Texas Symposium on Relativistic Astrophysics and Cosmology*, Vol. 759 of *Annals of the New York Academy of Sciences*, p. 291, The New York Academy of Sciences, New York

- Silant'ev, N. A. & Yakovlev, D. G. 1980, *Astrophys. Sp. Sci.*, **71**, 45.
- Thorsson, V., Prakash, M. & Lattimer, J. M. 1994, *Nucl Phys A*, **572**, 693.
- Tsuruta, S. 1979, *Phys. Rep.*, **56**, 237.
- Tsuruta, S., Canuto, V., Lodenquai, J. & Ruderman, M. 1972, *ApJ*, **176**, 739.
- Urpin, V. A. & Yakovlev, D. G. 1980, *Astrophysics*, **15**, 429.
- Van Riper, K. A. 1988, *ApJ*, **329**, 339.
- Van Riper, K. A. & Lamb, D. Q. 1981, *ApJL*, **244**, 13.
- Wiringa, R. B., Fiks, V. & Fabrocini, A. 1988, *Phys Rev C*, **38**, 100.
- Yakovlev, D. G. 1984, *Astrophys. Sp. Sci.*, **98**, 37.
- Yakovlev, D. G. & Urpin, V. A. 1980, *Soviet. Astr.*, **24**, 303.
- Yancopoulos, S., Hamilton, T. T. & Helfand, D. J. 1994, *ApJ*, **429**, 832.
- Zavlin, V. E., Pavlov, G. G., Shibano, Y. A. & Ventura, J. 1995, *A&A*, **297**, 441.

A XSPEC Models

Rather than present results for specific instruments and band passes, we supply our results in machine-readable form. We have calculated neutron star spectra for several values of R/R_s , and $\varphi = 0, \pi/2$. We assume a dipole field configuration and the $\cos^2\psi$ rule. The model is calculated for

$$T_{\text{eff},\infty}(\psi = 0) = T_{\text{eff}}(\psi = 0) \sqrt{1 - \frac{R_s}{R}} = 10^6 \text{K} \quad (57)$$

where $R_s = 2GM/c^2$. $T_{\text{eff},\infty}(\psi = 0)$ may be varied by applying a redshift and renormalization to the spectra. For ease of use by the x-ray astronomy community, we have created XSPEC table models with the data.

Within XSPEC, the models may be convolved with the response matrix for various x-ray instruments and compared with observed spectra. By using the redshift (z) and normalization (K) parameters we may obtain models for different effective temperatures and radii:

$$K = \left(\frac{R_{\infty, \text{km}}}{D_{10}} \right)^2 \left(\frac{T_{\text{eff},\infty}}{10^6 \text{ K}} \right)^3 \quad (58)$$

$$z = \frac{10^6 \text{ K}}{T_{\text{eff},\infty}} - 1 \quad (59)$$

where $R_{\infty, \text{km}}$ is the source radius in km as observed at infinity, *i.e.*

$$R_{\infty} = Re^{\Lambda_s} = R \left(1 - \frac{R_s}{R} \right)^{-1/2} \quad (60)$$

from Equation 55 and D_{10} is the distance to the neutron star in units of 10 kpc. This particular choice is consistent with the definition of the `bbodyrad` model in `XSPEC`.

Each additive model contains the single interpolation parameter R_s/R which ranges from 0 to 0.6601. As an illustration Figure 11 depicts one of the models convolved with the ROSAT PSPC response function for $R/R_s \rightarrow \infty$, $R = 20$ km and $D = 250$ pc with $N_H = 10^{20}$ cm $^{-2}$. Here, we have used the `wabs` model to calculate the interstellar absorption which assumes the Morrison & McCammon (1983) cross-sections.

The errorbars are calculated for an exposure of 10^4 seconds. For these parameters, the variation of the thermal flux with phase is apparent in the spectra. However, as we saw in the previous sections as R/R_s decreases, the variation in the thermal flux weakens.

The table models are available at the following URLs:

http://www.cco.caltech.edu/~jsheyl/analytic_ns/p0.fits for $\varphi = 0$
http://www.cco.caltech.edu/~jsheyl/analytic_ns/p90.fits for $\varphi = \pi/2$.

The `XSPEC` software itself is available at

<ftp://legacy.gsfc.nasa.gov/software/xanadu/>,

and an online manual is provided at

http://www.merate.mi.astro.it/~xanadu/xspec/u_manual.html.

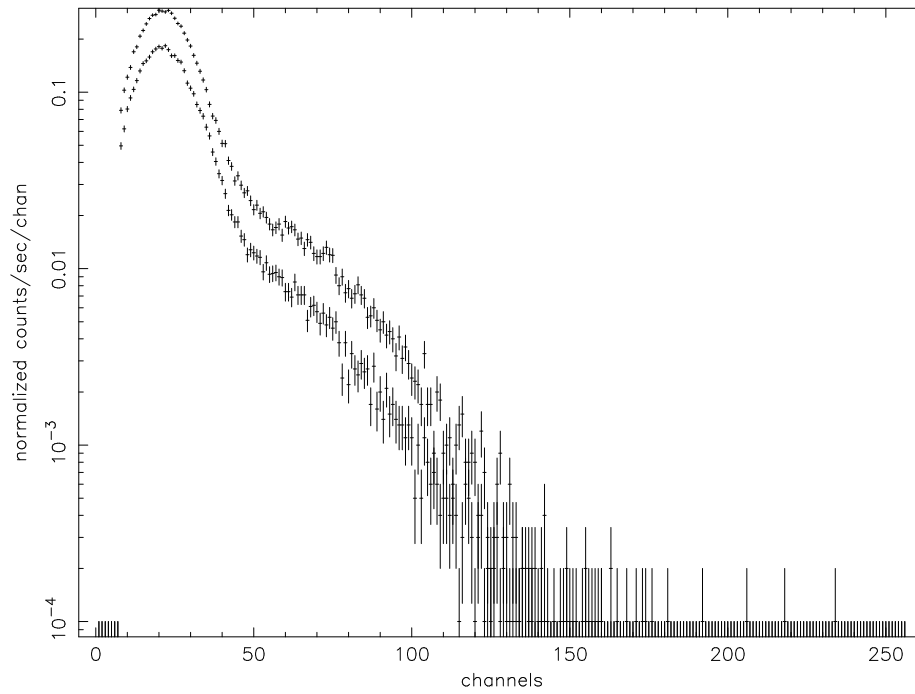


Figure 11: The calculated model spectra convolved with the ROSAT PSPC response matrix for $\varphi = 0$ (upper points) and $\varphi = \pi/2$ (lower points). The model parameters are described in the text. The errorbars are for an exposure of 10^4 s.